

Chapter 7

Light-sheet microscopy combined with remote force measurements

Show me a fish

— Anonymous

How multicellular organisms enact the morphogenetic programmes that ensure their characteristic forms remains an enigma. Genetic screens have yielded an array of essential structural, patterning and signaling pathways with which morphogenesis is orchestrated. [?] However, morphogenesis is ultimately a physical phenomenon that requires a physical explanation. *In vivo* imaging of morphogenesis allows measurements that reveal stereotypical patterns in the cellular behaviour by individual and groups of cells. These are indicative of active force generation but are insufficient to construct a quantitative explanation of where forces are generated and how forces propagate within and between tissues. To overcome these limitations, we require a quantitative characterisation of the physical properties of the tissues involved. Only with this knowledge are we able to understand how forces propagate within tissues to bring about morphogenesis. Measurements of the properties of individual cells [?] and for bulk tissues [?] have revealed both viscoelastic or viscoelasto-plastic solids. [?]. Bulk tissue properties can be estimated using atomic force microscopy to investigate a tissue surface. [?] Alternatively, micropipette aspiration can probe dissociated cells or explants, however deep tissue cannot be assessed directly. [?] More recently, techniques have been developed to measure tissue stress and viscoelastic properties, utilising laser ablation, oil droplets, or embedding tissue explants in matrix gel. Most recently, ferrofluid droplets have shown that local tissue

properties, that change regarding the tissue localisation. [?] There still a need for methods that can provide a repeated real-time readout of physical properties and relate those measurements to the underlying morphogenetic behaviour.

A method was needed that can give a non-destructive, quantitative measurement of local tissue physical properties at the length scale of a few cells, completed with seconds to minutes and repeatable over developmentally-significant periods. Biologically-compatible super-paramagnetic beads were chosen and implanted into the developing zebrafish embryos. A four-pole electromagnetic device was built that produces a controlled magnetic field gradient in 3D, such that a bead can be moved with known force. Tracking bead movement gives the dynamic material properties of the surrounding tissue. The emergence of the first cohesive tissue of the zebrafish blastula, between the “high” to “sphere” stages of development was then followed using this technique. After the mid-blastula transition, mesenchymal blastomeres become first motile and adherent to form the tissue that will go on to contribute to the first morphogenetic movement of the embryo. It was shown that a three-fold elevation of tissue elasticity and viscosity are associated with this development. This elevation is dependent upon E-cadherin-based adhesions and Rac-1 dependent cell protrusive activity, abrogating either interfered with these developmental changes. Interestingly, reducing Rho-kinase dependent cell contractility increased both tissue viscosity and elasticity and raised the number of cell protrusions. By using light-sheet microscopy in conjunction with magnetic tweezers allowed the fast image of volumes enough to track cells and their topology and their rearrangements; both cellular changes reduce as tissue elasticity and viscosity increase. Suggesting that the viscoelastic component predominantly to cell shape change and viscosity to cell rearrangement.

7.1 Tissue dynamics in developing organisms

7.1.1 *Danio Rario*

The zebrafish (*Danio rerio*) is a key model organism for vertebrate development. It shares features of its body plan and developmental stages with Xenopus, the chicken, and the mouse [?] (Wolpert et al, 2007) , indicating existence of conserved developmental mechanisms of interest. These mechanisms rely on organism-wide, reproducible patterns of cellular division, migration, death and differentiation,

Age / h	Stage	Notes
0 h	Zygote	Cytoplasm flows to the animal pole to form the blastodisc.
0.75 h	Cleavage	The blastodisc undergoes several rounds of rapid, synchronous, partial cleavage to give 64 blastomeres (and a yolk cell).
2.25 h	Blastula	The midblastula transition occurs; epiboly begins.
5.25 h	Gastrula	More cell migration. Gastrulation, involution, convergence, extension; forming the epiblast and hypoblast
10 h	Segmentation	The tail appears; somites develop; organogenesis starts.
24 h	Pharyngula	Circulation begins and pigmentation develops. The body axis straightens. Fins begin development.
48 h	Hatching	Primary organ systems complete morphogenesis, cartilage develops, the fish hatches.
72 h	Early larva	The swim bladder inflates; food-seeking behaviour occurs.

Table 7.1 Developmental stages of Zebrafish

which occur throughout the organism during development as well as adult life. As this cellular behaviour arises within the context of organism-wide signalling events, a truly complete understanding of the processes shaping them requires whole-organism imaging. Of the vertebrate model organisms, the zebrafish is best suited for whole organism imaging from fertilisation until hatching/birth. The embryo is transparent and small, but can still be physically manipulated, and develops outside the mother allowing for imaging uninhibited by surround tissue from the mother; as a result zebrafish require no external atmospheres to enable growth, unlike mice. Zebrafish growth is rapid, a single cell of a diameter of 0.7 mm becomes a 3.5 mm-long larva within three days (see Table 7.1). Finally, Zebrafish are suitable for genetic studies, the genome is fully sequenced and there exist tools for genetic manipulation. Breeding is simple, sexual maturity occurs at three months post fertilisation making for easy cross-breeding [?], and the costs of keeping zebrafish are lower than that of other vertebrates due to their low space requirements and minimal handler time. [?] (Lieschke & Currie, 2007).

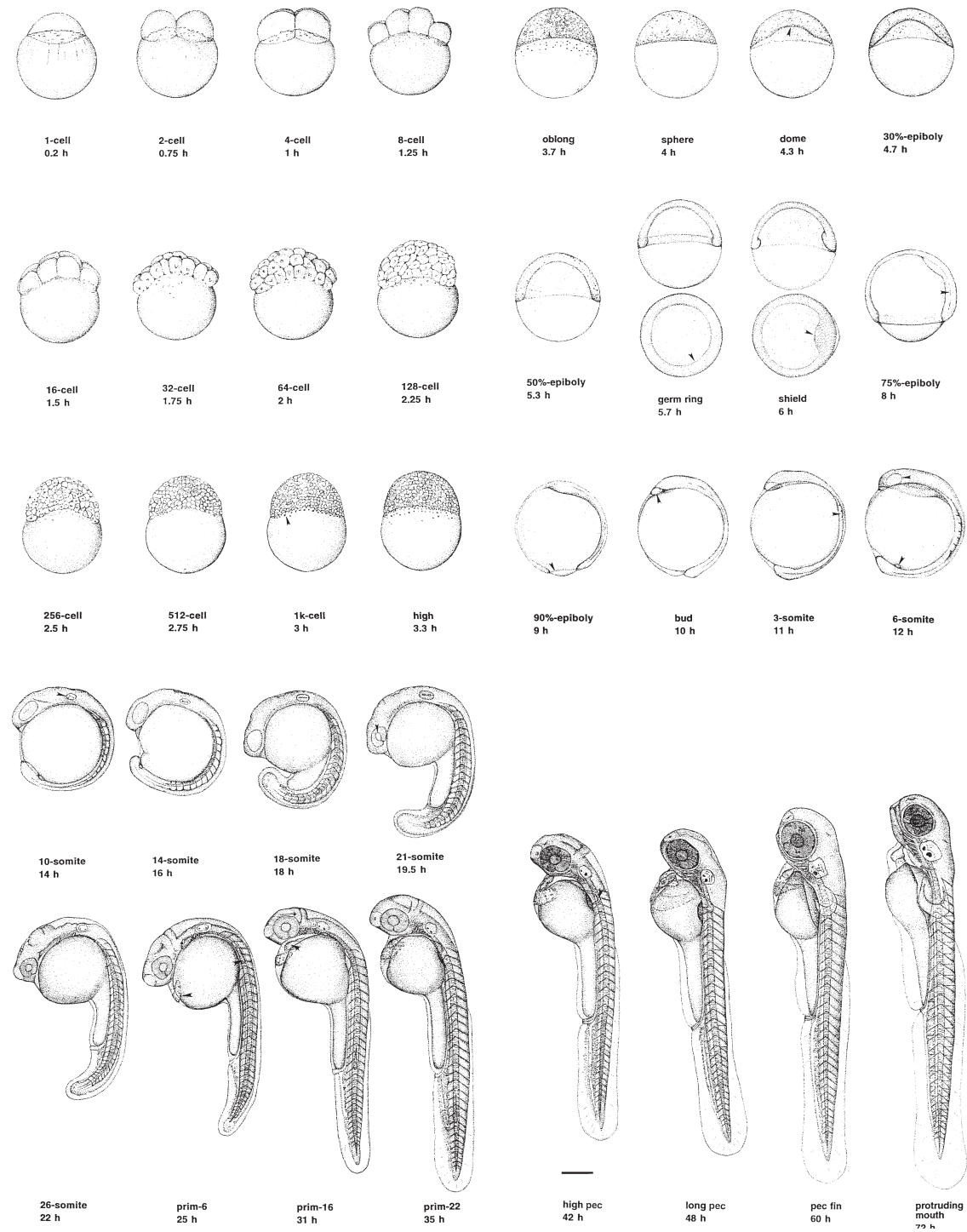


Fig. 7.1 Periods of embryonal development of the zebrafish. The embryo develops from a single cell into a larva in three days, undergoing morphologically apparent changes. See Table 7.1.

7.2 Methods of measuring tissue dynamics

The force generation requirements for the investigation of cellular morphogenesis greatly limits which techniques would be suitable for force application and it's measurement: the forces must be applied in the 10 μm -100 μm length scale, of a similar length to the size of a cell. The magnitude of these forces was needed to be in the 100 pm - 100 nm range, of a similar magnitude to the forces that we would expect the cells to be able to generate. [] It was also desirable for the process to result in minimal heat and light exposure to the organism, as well as to be minimally invasive. Immediately, potentially suitable techniques such as mechanical probing, atomic force microscopy, and optical tweezers prove intractable.

Magnetic tweezers operate under the principle of applying a force to a magnetic bead through a magnetic field gradient and are able to apply force at a distance, without perturbing biological materials, making the technique minimally invasive. Single-pole tweezer systems, where a single electromagnetic solenoid is able to apply a variable force on a bead in one direction, have been used in a number of experiments to understand the dynamics of cellular force responses. [] However, to fully characterise the force-generation in cellular rearrangement, it is necessary to generate a magnetic force in an arbitrary direction in three dimensions.

7.2.1 Magnetic tweezers

The design of the magnetic tweezers was based on the previously published design [?] (Vicci 2003), which is compatible with large sample like zebrafish embryo and was shown to generate sufficient forces using COMSOL simulations. This section presents the development of the magnetic tweezers including the imaging chamber required by the LSFM. The mechanical design of the magnetic tweezers was based on a monopole model. In this simplification the magnetic field is assumed to be generated by point sources (monopoles) around a sample containing a magnetic bead. The sum of the aggregated monopole strengths must equal to zero because, in nature, there are no actual sources or sinks of magnetic flux (i.e. solenoids generate dipole magnetisation). In this model, a force acting on the bead in the direction of a monopole can be approximated by [?] The magnetic dipole moment \mathbf{m} induced in the bead by a magnetic field B is given by:

$$\mathbf{m} = \chi \mathbf{B}$$

$$\mathbf{m} = \frac{\pi d^3}{2\mu_0} \frac{\mu_r - 1}{\mu_r + 2} \mathbf{B} \quad (7.1)$$

A force, proportional to the magnetic dipole moment, is then exerted on the bead in the presence of magnetic field gradients

$$\mathbf{F} = \frac{\pi d^3}{2\mu_0} \frac{\mu_r - 1}{\mu_r + 2} \nabla \mathbf{B}^2 \quad (7.2)$$

where d is the diameter of the bead, μ_0 is the magnetic permeability of free space, μ_r is the relative magnetic permeability of the bead and \mathbf{B} is the magnitude of the field generated by a magnetic monopole. \mathbf{B} is in the form of $\frac{B_p}{r^2}$ where B_p is the monopole strength and r is the distance from the monopole. Hence the gradient $\nabla \mathbf{B}$ of the field is $2\frac{B_p}{r^3}$ and the force on the bead proportional to $2\frac{B_p^2}{r^5}$ [?] (Vicci 2003). In the mechanical design of the magnetic tweezers, it was thus desirable to position magnetic poles as close as possible to a sample.

A minimum of four monopoles is required to achieve effective 3D specification of the force acting on the bead. The optimal configuration is a tetrahedral geometry, where monopoles are distributed on the vertices of a tetrahedron. Deviation from this geometry limits the range and directionality of achievable forces. Finally, only a single bead should be used at a time, as agglomeration of beads influences the magnetic field distribution due to the interactions between the beads, and thus disturbs the monopole model [] The magnitudes and gradients of the magnetic

field in the space between the poles is controlled by four solenoid coils; by varying the currents in these coils independently, one may control the the magnitude and direction and magnitude of the force acting on the bead.

Model Theory

The simplest phenomenological model capable of mimicing the viscoelastic response of an developmentally early Zebrafish embryo, subject to stress generated by a moving spherical rigid object, is a one-dimensional linear combination of elastic spring and viscous dash-pots. More precisely, the model assumes a parallel spring and dash-pot [(Kelvin\IeC {-}Voigt model)], in series with a second dash-pot, see Figure 7.2

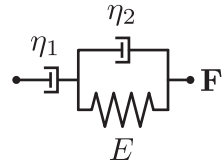


Fig. 7.2 Viscoelastic model used for embryonic tissue used in this work; consisting of a dashpot in series with a dash-pot and spring in parallel. The spring E represents the stiffness of the ensemble tissue, the first dashpot (η_1) represents tissue viscosity, the second dashpot (η_2) represents cellular viscosity.

The model is described by the following parameters: dynamic viscosities η_1 and η_2 and elastic stiffness E . When a stress σ is applied, the spherical rigid object, in this case a magnetic bead made of suparparamagnetic nanoparticles embedded into a polyester matrix, moves and the displacement is quantified by the strain ϵ . The same parameter is used to evaluate the recovery phase, when $\epsilon = 0$. The experimental protocol used here consists from two phases: the creep phase where from equilibrium state, at $t = 0$, a constant force is applied instantaneous on the bead and kept for a given time t_1 (60 s), and the recovery phase where the force is removed at t_1 and the bead displacement is monitored for sufficient time (120 s). To model the equations of motion the a linear spring is described by:

$$\epsilon = \frac{1}{E}\sigma \quad (7.3)$$

while a dash-pot obeys:

$$\dot{\epsilon} = \frac{1}{\eta}\sigma \quad (7.4)$$

The equation for a spring and a dash-pot connected in parallel follows as:

$$\sigma = \sigma_E + \sigma_{\eta_2} = E\epsilon_p + \eta_2\dot{\epsilon}_p \quad (7.5)$$

$$\ln \left(\frac{\sigma}{\eta_2} - \frac{E}{\eta_2}\epsilon_p \right) = -\frac{E}{\eta_2}t + \ln C_1 \quad (7.6)$$

Setting the initial conditions of $\epsilon_p = 0$ at $t = 0$:

$$\epsilon_p = \frac{\sigma}{E} \left(1 - \exp\left(-\frac{E}{\eta_2} t\right) \right) \quad (7.7)$$

The temporal variation of the dash-pot is ruled by:

$$\sigma = \eta_1 \dot{\epsilon}_s \implies \epsilon_s = \frac{\sigma}{\eta_1} t \quad (7.8)$$

Knowing that $\epsilon = \epsilon_s + \epsilon_p$, The strain variance is therefore:

$$\epsilon = \frac{\sigma}{\eta_1} t + \frac{\sigma}{E} \left(1 - \exp\left(-\frac{E}{\eta_2} t\right) \right) \quad (7.9)$$

During the second phase, that starts at t_1 , the force becomes zero $\sigma = 0$ and the total strain is given by the previous displacement of η_1 dash-pot blocked at $t = t_1$ plus the relaxation of Kelvin-Voigt model. The later is described by:

$$E\epsilon_p + \eta_2 \dot{\epsilon}_p = 0 \implies \epsilon_p = C_2 \exp\left(-\frac{E}{\eta_2} t\right) \quad (7.10)$$

From the continuity of strain and $t = t_1$, C_2 becomes:

$$\frac{\sigma}{\eta_1} t + \frac{\sigma}{E} \left(1 - \exp\left(-\frac{E}{\eta_2} t_1\right) \right) = C_2 \exp\left(-\frac{E}{\eta_2} t\right) \quad (7.11)$$

$$C_2 = \frac{\sigma}{E} \left(\exp\left(\frac{E}{\eta_2} t_1\right) - 1 \right) \quad (7.12)$$

So, for $t \geq t_1$ the strain is:

$$\epsilon = \frac{\sigma}{\eta_1} t_1 + \frac{\sigma}{E} \left(\exp\left(\frac{E}{\eta_2} t_1\right) - 1 \right) \exp\left(-\frac{E}{\eta_2} t\right) \quad (7.13)$$

The equations of motion may be summarised as

$$\epsilon = \begin{cases} \frac{\sigma}{\eta_1} t + \frac{\sigma}{E} \left(1 - \exp\left(-\frac{t}{\tau_2}\right) \right) & \text{for } t \geq t_1 \\ \frac{\sigma}{\eta_1} t_1 + \frac{\sigma}{E} \left(\exp\left(\frac{t_1}{\tau_2}\right) - 1 \right) \exp\left(-\frac{t}{\tau_2}\right) & \text{for } t \leq t_1 \end{cases} \quad (7.14)$$

where $\tau_2 = \frac{\eta_2}{E}$

A bead moving through a viscous fluid could be described by Stokes' law $F = 6\pi\eta'r\nu$, where r is the radius of the bead and ν it's critical velocity. Stoke' law may be written as:

$$F = 6\pi\eta'r \frac{dx}{dt} \quad (7.15)$$

$$\implies \frac{F}{\pi r^2} = 6\eta' \frac{d}{dt} \frac{x}{r} \quad (7.16)$$

$$\implies \sigma = 6\eta' \frac{\epsilon}{dt} \quad (7.17)$$

The equation of a dash-pot $\dot{\epsilon} = \frac{\sigma}{\eta}$

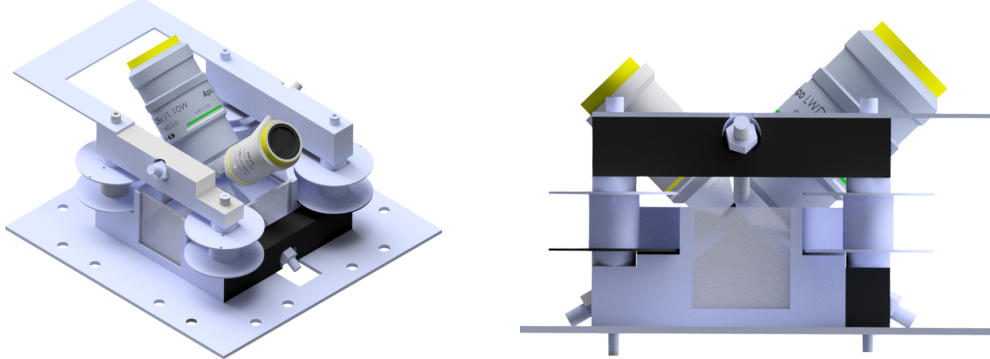
$$(7.18)$$

To model the elastic spring, the elastic response of the tissue due to the bead displacement is approximated by the Thomson's solution of a point force in an infinite isotropic medium [1] The displacement \mathbf{u} in cylindrical coordinates (p, z) for a point force F_z located at the origin and directed along z axis is given by:

$$\mathbf{u} = \frac{F_z}{4\pi\mu r} \left[\frac{pz}{4(1-v)r^2} \hat{\mathbf{p}} + \left(1 - \frac{p^2}{4(1-v)r^2} \right) \hat{\mathbf{z}} \right] \quad (7.19)$$

Where $\hat{\mathbf{p}}$ and $\hat{\mathbf{z}}$ are unit vectors, μ is the shear modulus (deformation at constant volume) and v is Poisson's ratio (negative ratio of transverse to axial strain of a specimen under an axial force). As only forces in the $\hat{\mathbf{z}}$ direction are being considering, Equation (7.19) becomes:

$$u_z = \frac{F_z}{4\pi\mu r} \left[\left(1 - \frac{p^2}{4(1-v)r^2} \right) \right] \quad (7.20)$$



(a) Light-sheet objective placed within (b) Side view with magnetic centre of the magnetic tweezer chamber. tweezers at the double focus of the excitation and detection objective.

Fig. 7.3 CAD designs of the magnetic tweezer housing coupled to the light-sheet objectives.

Evaluating the displacement only on z axis where $p = 0$, reduces this to:

$$\nabla z = \frac{F_z}{4\pi\mu r} \quad (7.21)$$

In the close proximity of the bead of radius r_{bead} , the displacement is given by:

$$\frac{\nabla z}{r_{\text{bead}}} = \frac{1}{4\mu} \frac{F_z}{\pi r_{\text{bead}}^2} \implies \epsilon = \frac{1}{4\mu} \sigma \quad (7.22)$$

Which is equivalent to (7.3) when substituting E with 4μ

$$(7.23)$$

7.2.2 Magnetic tweezer design

A square loop of iron was used carry magnetic flux from four solenoids to four embedded magnetic tips. The lower magnetic tips were mounted at 30° azimuthally, this allowed for the very large 1.1 NA, long working distance Nikon objective to image the magnetic centre of the magnetic poles. This orientation of tweezer poles does however leave the design without 10% of the maximum magnetic field strength that a 45° pole mounting would provide (2.33 T).

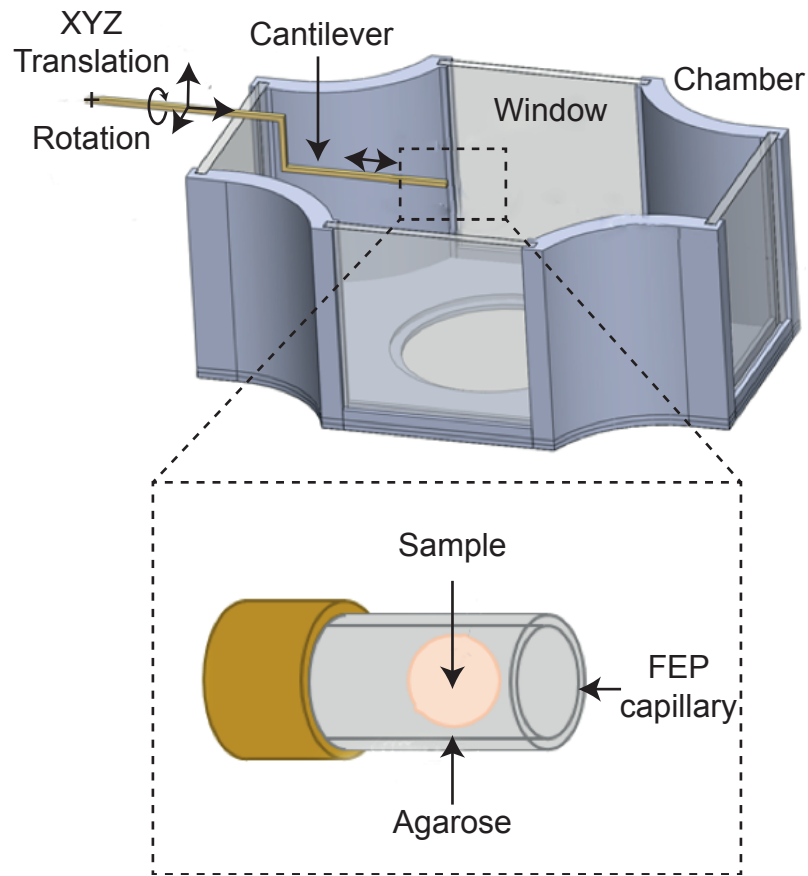


Fig. 7.4 3D printed chamber for housing the magnetic tweezers whilst providing ambient living conditions for a developing Zebrafish.

Imaging Chamber Design

The imaging chamber presented was 3D printed in ABS (Acrylonitrile butadiene styrene) to allow for modular and rapid re-design. Clear acrylic windows were added to allow for a positioning camera (PiCam) to be placed below the tweezer system, this aided with the positioning of the Zebrafish. The chamber was water tight and featured heating pads to maintain the embryo medium and Zebrafish at a comfortable 28.5 °C during imaging.

Force calibration

3D magnetic field gradient is shaped by a combination of currents to obtain forces of range of 8 nN. Force calibration was realised by analysing the velocities of a 41.17 µm diameter paramagnetic bead in known viscosity silicone oil at different combination of intensities of currents. The coordinate systems of the Magnetic tweezers and

the light-sheet system were required to be aligned due to the non-linear decline of force of the magnetic field away from the magnetic centre. This was achieved by defining an origin within the tweezer system itself, where force in every direction was maximal. This point was then recorded by carefully inserting a fiducial magnetic bead attached to an arm and positioned using micrometer screws. Once the tweezer system was fixed to the light-sheet system, the automated stage was carefully driven such that the fiducial bead was at the imaging centre of the camera and the axial centre of the Piezo objective actuator. The tweezer positioning was coarse positioned by eye using the automated stage, fine correction followed by utilising the bright-field imaging built into the sample chamber.

Synchronisation

The magnetic tweezers were calibrated and automated using current amplifiers driven by voltages from a Raspberry Pi. Simple RS232 commands could control the amount of force, direction and on/off state of the tweezers. These commands were then sent from the LabVIEW controller controlling the light-sheet system to ensure good synchronisation between the initial drive of the bead and the start of the volume acquisition.

7.3 Algorithmic bead tracking

To perform a model fitting as derived in (7.14) the magnetic bead needed to be tracked algorithmically. Each volume was $2048 \times 2048 \times 100$ voxels, with each volume acquisition taking 5 seconds. Each push-pull experiment produced 42 x,y,z spatial coordinates in time, hence the entire data set to be analysed was 172 GB. Two methods of bead tracking were explored, slice-wise Hough transform analysis and template matching.

Hough-based

The Hough transform is a featuring tracking mechanism used to transform an image into a space whereby intensity minima or maxima represent circles. These localised maxima then correspond to multiple circles in the image space of a given range of radii as provided to the function. The first iteration of the analysis algorithm would exhaustively search for circles with varying threshold sensitivity until a single circle

was found of the correct radius through the image volume. Once singular circles were found slice-wise, a circle was fit to the radii found in each slice to localise the sphere in z . This lead to multiple computational expensive transforms being applied and the algorithm being slow. It is possible to use 3D Hough transform that searches for spheres rather than circles; again, multiple matches are likely to be returned resulting tracking errors.

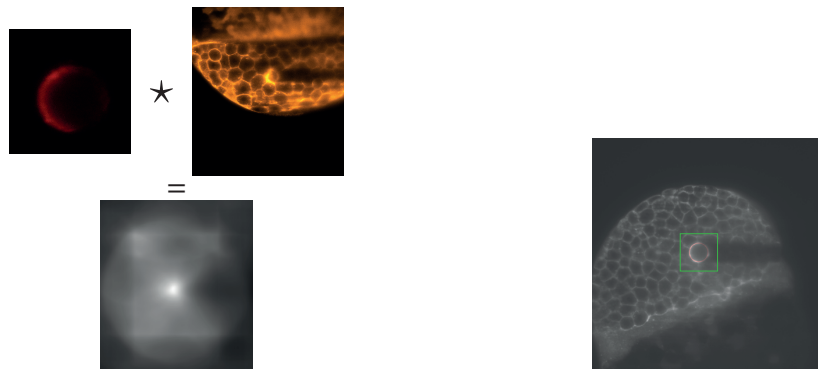
7.3.1 Template matching

As only a single sphere could be found in each image volume, a template-matching approach as explored. Initially an *ideal bead* was extracted from an image volume for future analyses (see Figure 7.5a). However, it was found empirically that the ideal bead volume was more likely to chase cells more so than a virtual idealised bead. To construct a virtual bead, a virtual volume would be constructed and a white hollow sphere of the correct pixel radius (160 px) would be superimposed.

Templating matching techniques fundamentally rely on the cross-correlation of two images or volumes. Cross-correlation is made programmatically quicker by operating in Fourier space for convolution rather than iteratively in image space. Though this does decrease the overall computation time, the overall memory usage of the algorithm will increase. As such care has to be taken to avoid Random Access Memory (RAM) overfilling as this can either cause the algorithm to crash. Particularly in operating systems without a well managed swap-space; or, the swap-space is used and the algorithm becomes very slow as it reads large Fourier space volumes on and off of a slower hard-drive.

To circumvent large amounts of memory being used a windowing technique was employed to ensure a minimal amount of voxels needed were being analysed. The cuboidal window was set to be double the radius in each dimension, this was arbitrarily set with the assumption that the bead would not move out of the window between concurrent two time points. Between each frame the centre of the window would be shifted to be aligned with the centre of the bead. The voxels within this window were analysed and the window shifted again by the relevant offset. The bead centres in 3D were then exported to a text file for analysis.

The seed location in the first frame for the bead was found one of two ways. A best guess of bead location was found by downsampling the resolution of the image stack and performing a template match on the stack, a finer search would



(a) Template matching of an ideal fluorescent bead with a volume of Zebrafish produces a volume image with a single maximum peak of where the bead resides

(b) Here, the red circle represents a well localised single bead.

Fig. 7.5 Template matching used to localise bead positions through time and in 3D.

be performed after and the algorithm as described above would continue. As the bead was comparable to the size of cells within the Zebrafish, downsampling would sometimes cause the algorithm to fail. Each time series was checked visually at the output, where the window (Green) would follow the bead (Circled red) 7.5a. If a time series was seen to fail (and likely at the first frame), the second technique would be employed whereby a user would manually position the initial window to ensure the fine fast tracking could continue. All trajectories in which cells adjacent to the bead underwent cell division or large autonomous displacements were excluded.

Sub-pixel tracking

The output of the cross correlation of a template and an image volume will have a maxima at the position where correlation is the highest. For the described algorithm the highest peak is the most likely candidate for a bead being matched. As such, the simplest way of tracking a bead in a window requires returning the cartesian coordinates of that largest pixel. However, the pixel values in the immediate vicinity of the highest pixel value will steadily ramp up. By fitting a smooth Gaussian local to the maximal peak a sub-pixel resolved series of coordinates may be found. More complicated but more accurate technique for sub-pixel tracking involves the fitting of an b-spline. The result of a spline fitting offers a smooth fit to what is assumed continuous smooth data, the spline itself will interpolate the underlying data. To this end large bead positioning accuracy can reach beyond the diffraction limit.

7.3.2 Cell tracking

The actions of nearby cells with regard to the bead being moved were also of importance, to track their movements and deformation a 3D watershed algorithm written in IDL was applied to membrane-only data imaging data. Having a two-colour Zebrafish whereby one channel was fluorescent in the nuclei whilst another exclusively in membranes was considered. However, the time resolution would have needed to have been halved to allow for this given the system constraints. Alternatively having a dichroic image splitter or an additional camera to be added was possible. This approach would have halved the overall image resolution in the y axis and an additional camera would have been a time-costly as well as monetarily expensive solution.

7.4 Results

7.4.1 Micro-rheology reveals increase in physical parameters during high- to-sphere- stage transformation

Even though it has been speculated that morphogenetic change must depend upon changes in the physical properties of tissues, there is little direct evidence to support this idea. We wish to ask if the changes that we see in cell movements and protrusive activity during the high- to sphere-stage transformation are accompanied by a modulation of physical properties of the blastoderm. To address this question, magnetic tweezers were used to apply a direct and known force to a 40 $40\text{ }\mu\text{m}$ diameter super paramagnetic bead implanted into the blastoderm [].(

Beads were implanted and them and the cells surrounding them were image in blastula-stage embryos for extensive periods (up to 8 hours) and detected no changes in local cell arrangement, actin cytoskeleton organisation or myosin localisation around the beads. Embryos containing a bead developed unperturbed by its presence. The physical properties of the tissue were measured by applying a calibrated, constant force (in the order of 8 nm) for 1 min and tracking the displacement of the bead during and after application. Force was directed alternately radially towards or away from the yolk at 3 min intervals. Bead trajectories reveal that embryonic tissue acts as a viscoelastic medium. Trajectories invariably show an initial fast displacement followed by a slower, linear displacement or creep, see Figure ???. Upon

release, the bead recoils rapidly towards its original position in a reversal of the initial fast displacement. Displacement during the slower creep phase is not recovered, see Figure ???. Between high- to sphere-stage there was a significant and systematic reduction in the magnitudes of all phases of movement but not in the overall shapes of these trajectories, see Figure ???. To quantify and further characterise these findings, a parameterised mechanical model (7.14) that accounts for the shapes of bead trajectories over time was fit. The most parsimonious model consists of a dashpot in series with parallel spring and dashpot, see Figure 7.2. The dashpots are characterised by viscous coefficients η_1 and η_2 , and the spring by an elastic modulus, E. Fitted parameters reveal that E increased by 3 fold ($E_{0\text{ min}}=2.61 \pm 0.57 \text{ Pa}$; $E_{75\text{ min}}=7.98 \pm 2.50 \text{ Pa}$) and η_1 1.8 fold ($\eta_{1,0\text{ min}}=156.1 \pm 58.3 \text{ Pa s}$; $\eta_{1,75\text{ min}}=286.85 \pm 69.34 \text{ Pa s}$) and η_2 2.5 fold ($\eta_{2,0\text{ min}}=15.82 \pm 3.20 \text{ Pa s}$; $\eta_{2,75\text{ min}}=40.20 \pm 10.74 \text{ Pa s}$) over a development time of 75 min. No significant differences were found between the two directions of force application ($p_E > 0.05$, $p_{\eta_1} > 0.05$, $p_{\eta_2} > 0.05$). This trend was seen irrespective of the starting developmental age of the embryo, excluding the likelihood of work hardening as an explanation. A characteristic time constant of the elastic deformation, τ , can be derived from the ratio of η_2 to E. Despite large changes in both of η_2 and E, τ remains relatively constant over developmental time (mean = 5.33 s). This suggests that this tissue may contain a mechanism of self-regulation of τ or that both E and η_2 are determined by a common feature.

The proposed mechanical models provides a good explanation for the trajectory of the bead during the active force application and the initial recoil period. However, bead movements in the later recovery period are more erratic and not accounted for by the model. Potentially, these deviations may result from additional processes, such as active cell movements.

The fitted mechanical model implies that the tissue can be described by two mechanical elements, a soft viscoelastic component and a pure viscous component. A simple hypothesis would be that the viscoelastic component derives from the mechanics of individual cells, and the purely viscosity component is a measure of cell-cell interaction. This was addressed in two ways. Firstly, changes in cell shapes and rearrangements within the tissue during and after bead movement were visualised and measured; secondly, these measurements were repeated in embryos in which there had been a manipulation of cell adhesion, cell protrusive activity and cell contractility testing their roles in determining mechanical properties.

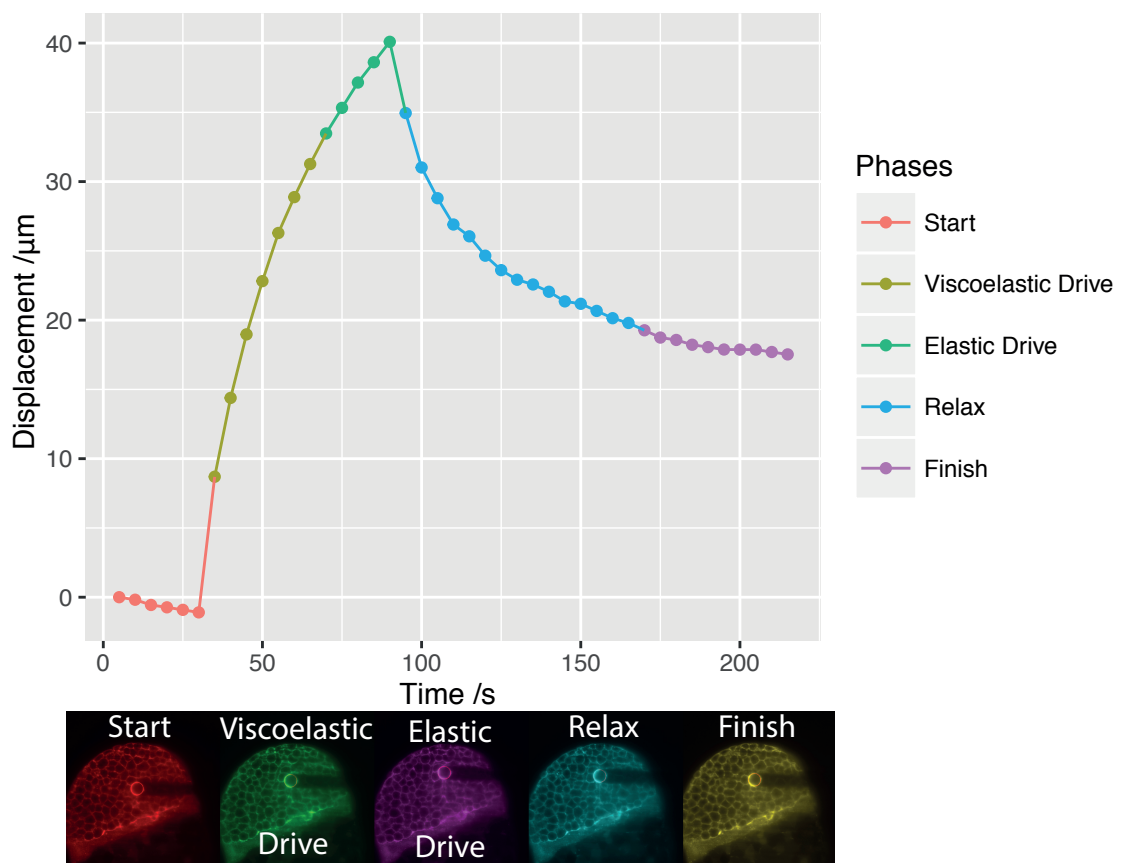
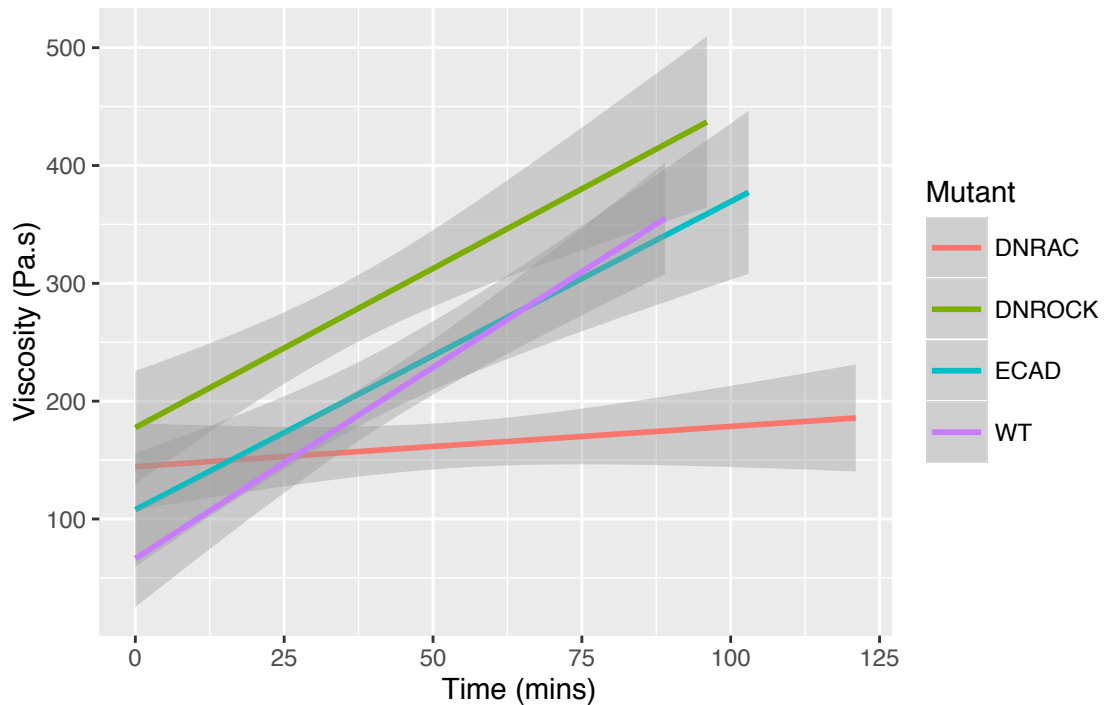
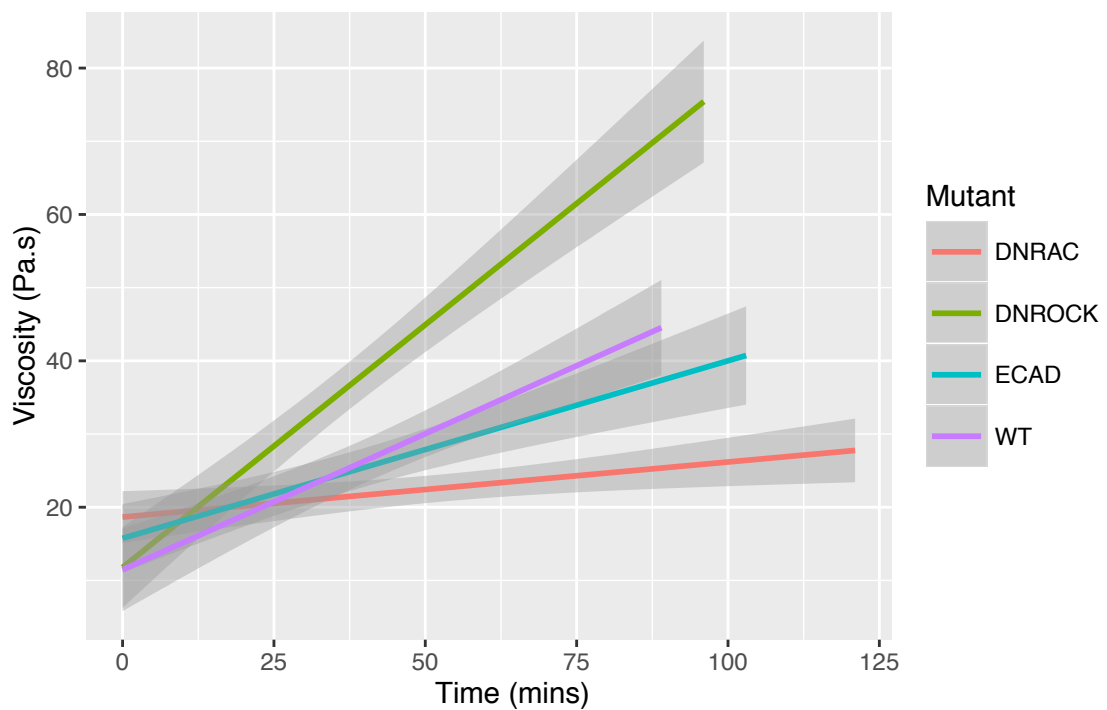
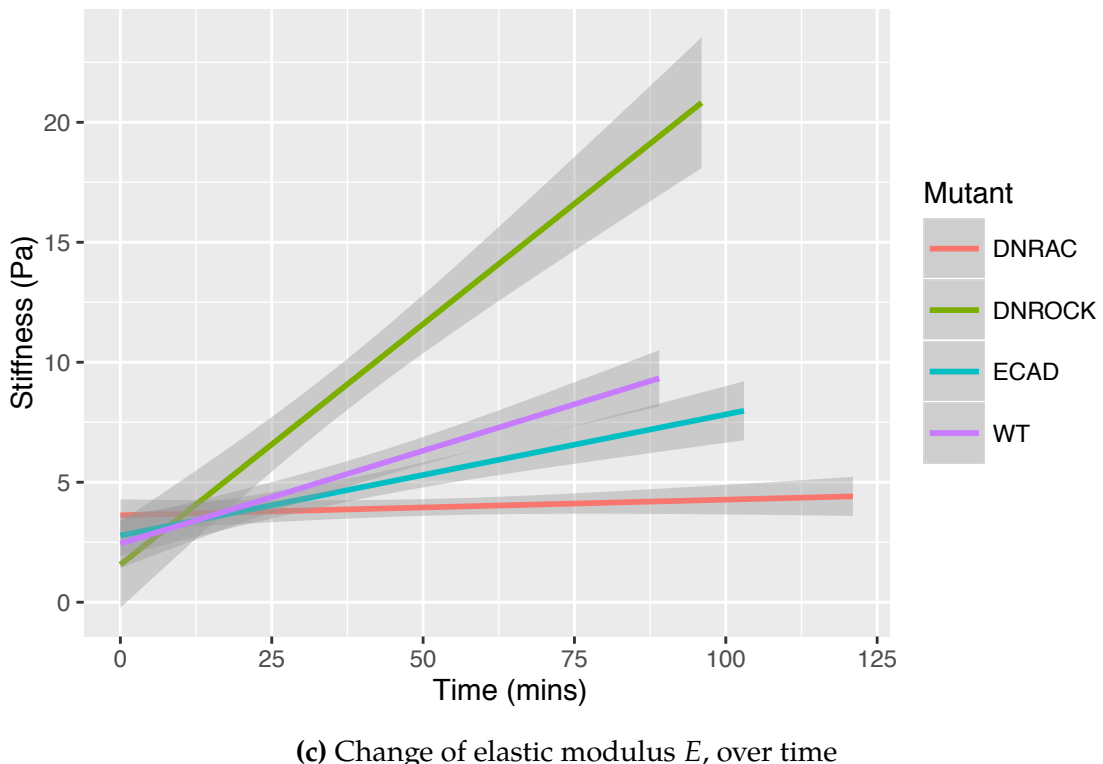


Fig. 7.6 Paramagnetic bead moved within embryonic tissue by a known force show a trajectory characteristic of viscoelastic behaviour, with a rapid elastic response (*elastic* phase), followed by a linear creep period (*creep* phase). When the force is removed, the bead is recoiled (*recoil* phase).

(a) Change of cellular viscosity η_1 , over time(b) Change of tissue viscosity η_2 over time



(c) Change of elastic modulus E , over time

Fig. 7.7 These knock downs have consequences on the developmental evolution of rheological parameters, viscosity coefficients η_1 7.7a and η_2 (7.7b), and, elastic modulus E (7.7c): they are decreased in MoECad ($n=151$ pulls, 9 embryos), and DNRAC ($n=158$ pulls, 9 embryos) while they are increased in DNROCK ($n=107$ pulls, 9 embryos) compared to WT ($n=178$ pulls, 9 embryos).

7.4.2 Elasticity is linked with cell shape deformation and Viscosity with cell rearrangement.

To examine how cells around the bead responded during the force application, fast volumetric light-sheet imaging combined with magnetic tweezers enabled the simultaneously tracking of cell shapes and positions during mechanical probing (Figure 7.8 A-B). The time course was partitioned into five epochs, based upon the experimental protocol and the mechanical signatures as described above. The elastic phase is defined as $3 \times \tau$ (spanning 95% of the elastic duration). The remaining period of active bead displacement is defined as the creep phase. Thirdly, a 3τ period of elastic recoil was analysed as the recoil period. Cell outlines and positions were automatically tracked and manually omitted and corrected. Cell shape changes and cell displacements are measured along the axis of force application to the bead. Four sectors were defined around the bead relative to this axis (Figure 7.8 A); here only the front and rear sectors are considered. In front of the bead, during the elastic period, cells are both compressed and displaced forward by its movement (Figure 7.8 C,D). This tendency of cells to deform diminishes over development time (Figure 7.8 F, $p_{\text{linear-regression}} = 0.016$). In fact, cell shape strain rates are highly correlated with and largely accounts for tissue deformation strain rate (Figure 7.8 F, $p_{\text{correlation}} = 0.0001757$, $R^2 = 0.743$). Cell shape strain rate coefficient is correlated with E (Figure 7.8 I, $p_{\text{correlation}} = 0.0449$, $R^2 = -0.453$). Behind the bead, we can see a complementary pattern of cell and tissue stretching ($R^2 = 0.473$, $p = 0.0748$), at all except the earliest developmental stages. Incomplete cell adhesions which in turn create holes in the tissue when the bead moves with excess force, may be the cause of this effect. For these cases, cell shape change strain rates are not correlated with tissue deformation strain rate. When the magnetic force is no longer applied, previously compressed cells ahead of the bead re-expand back along the force axis (Figure 7.8 D,H). Previously stretched cells behind the bead would then contract as the bead recoiled backwards (Figure 7.8 D). There is a strong correlation between E and the rate of expansive cell shape deformation in front of the bead (Figure 7.8 K, $R^2 = 0.53$, $p = 0.016$). This is consistent with the rapid elastic bead recoil being determined by an elastic recoil in cell shape, after the release of the imposed force. In conclusion the cellular signature of the elastic periods are largely accounted for by cell shape deformations.

7.4 Results

105

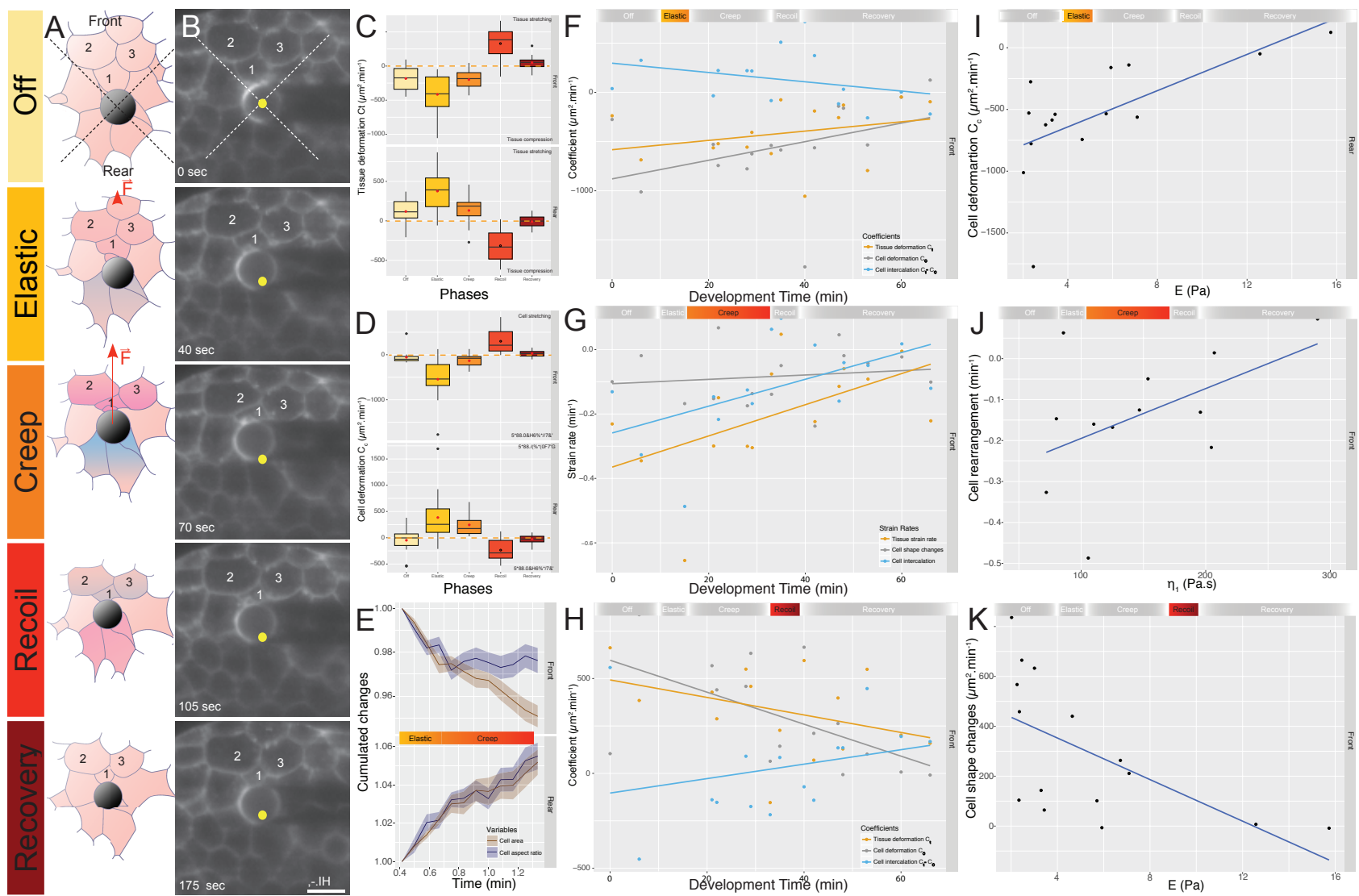


Fig. 7.8 p.t.o

Fig. 7.8 A-B: Sketch of typical rheological experiment (A) in WT embryo under SPIM (B) where blue represents cell extension and red is compression. 1-2-3 label regarding cells over time-lapse. Yellow dot marks the original position of the bead centre. C-D: Analysis of the coefficient of deformations C_t and C_c shows that tissue (C) and cells (D) are compressed at the front of the bead while they are stretched at the rear during bead pulling ($n = 14$ pulls, 3 embryos). E-H: Analysis of cell area and cell aspect ratio reveals cells disappear from imaging plane, suggesting cells at the front rearrange in 3D, while at rear, cells are stretched (E). Along developmental time, tissue deformation (C_t), cells deformation (C_c) and cell intercalation ($C_t - C_s$) during elastic phase (in $\mu\text{m}^2 \text{min}^{-1}$), at the front of the bead, show that tissue compression can be accounted mainly by cell shape changes (F), while, during creep phase, strain rates show that this accountancy is lost, suggesting cell rearrangement is major event (G). When force is released, cells at the front relax to their original shape (H). I-K: Correlation analysis of cell parameters and rheological parameters. This is supported by correlations between elastic modulus E and cell shape change coefficient during elastic phase, at the front of the bead (I), between viscosity coefficient η_1 and cell rearrangement rate during creep phase (J), between elastic modulus E and cell shape change coefficient during recoil phase (K). Lines represent linear regressions.

To investigate how tissue deforms during the creep phase, which in the mechanical model is defined by η_1 , the behaviour of cells in the tissue at the front and rear of the bead were visually inspected. Cells became more compressed and would move out of the plane (decreasing in area), in front of the bead and conversely cells would become stretched and enter the plane at the rear (Figure 7.8 A, B). This behaviour may be quantified by comparing changes in cell aspect ratio and area through both the elastic and creep periods (Figure 7.8 E). Early cell shape changes give way to area changes during the creep period, this may be interpreted as the result of cells rearranging in the tissue in front and behind the bead.

While the elastic periods were dominated by changes in cell shape, the creep period is characterised by cell rearrangements. Cell shape strain accounts for a small fraction of tissue strain rate (Figure 7.8 G), and does not correlate with η_1 ($R^2_{\text{front}} = 0.345, p = 0.21$; $R^2_{\text{rear}} = -0.052, p = 0.85$). Nonetheless, measurable cell shape strain rates indicate that some contribution persists through the creep period. However, cell intercalation strain rate does correlate with η_1 , both in front (Figure 7.8 J) $p_{\text{correlation}} = 0.0638, R^2 = 0.49$) and behind the bead ($p = 0.035$, correlation = -0.546). Cell rearrangements appear to be the major determinants of tissue viscosity in the creep period.

7.4.3 Modifications of cell motility and migration lead to defects in early embryogenesis and tissue rheology.

The results of analysing movement during bead displacement are consistent with our simple hypothesis of a two-component model. These changes affect embryo development, and the mechanical properties of the blastoderm. Cell adhesion is a fundamental requirement for building a cohesive tissue, expression of E-Cadherin (*cdh1*) was reduced. Using a knock-down Morpholino approach (MoECad) for cell adhesion leads to embryos defective in the high-to-sphere transformation; these embryos failed to achieve a spherical shape (Figure 7.8 A). Rheological measurements show that MoECad-treated embryos remain less stiff and less viscous than their wildtype counterparts. Further, they are reduced in the elevation of these properties over developmental time 7.7 Developmental trends are significantly different to WT, $p_E = 5.63 \times 10^{-7}$, $p_{\eta_1} = 2.10 \times 10^{-3}$, $p_{\eta_2} = 0.042$.

Cell migration and cell protrusive activity are two major cell behaviours at these stages. Small GTPases are identified as central orchestrators of cell polarity and motility [1] Two complementary molecular components of cell migration, Rac1 signalling were manipulated, Rac1 signalling using a dominant-negative Rac1 construct (DNRAC, [1]), RhoA signalling by a dominant-negative Rho-kinase construct (DNROCK, [1]). Speculatively, DNRAC should eliminate protrusive activity, while DNROCK would reduce the activation of the molecular motor myosin-2. The injection of these dominant negative constructs affects early morphogenesis, DNRAC-injected embryos fail to progress to a spherical shape, while DNROCK injection causes a faster round-up of the embryo. When we measure those rheological parameters by magnetic bead displacement, we confirm these predictions: DNRAC embryos fail to increase stiffness and viscosities η_1 and η_2 ($p_E = 1.016 \times 10^{-9}$, $p_{\eta_1} = 1.876 \times 10^{-4}$, $p_{\eta_2} = 0.0028$) while DNROCK embryos become stiffer and more viscous ($p_E = 7.59 \times 10^{-25}$, $p_{\eta_1} = 6.74 \times 10^{-15}$, $p_{\eta_2} = 3.65 \times 10^{-12}$) than their WT counterparts (Figure .F-H). Interestingly, τ is affected by the different knock downs, stiffer embryo showing a shorter τ than softer ones ($p \ll 1 \times 10^{-5}$).

How do the changes rheological properties found for DNRAC and DNROCK treatments are reflected in the rates of cell and tissue deformation?

Fast light sheet imaging analyses were repeated with each knock-down treatment, to follow cell behaviours during force application. The resultant parameters do

segregate according to their mechanical properties: softer DNRAC embryos present more cell deformation during the elastic period ($p_{WT-DNRAC} = 0.0013$) and more cell rearrangement during the creep period ($p_{WT-DNRAC} = 0.0025$), compared to WT. Cells in the stiffer DNROCK-injected embryos deform less in the elastic period ($p_{WT-DNROCK} = 0.0017$) and induce fewer cell rearrangements in the creep period ($p_{WT-DNROCK} = 0.0013$) (Figure 7.8 J). These results confirm that the previously-observed correlations between cellular and rheological parameters hold true under this expanded range. Stiffness E is strongly correlated with initial cell shape deformation while η_1 is strongly correlated with cell rearrangements. This suggests that there may be a relatively simple cellular interpretation of the physical model measured using magnetic bead rheology.

7.4.4 Biological methodology

Embryos were harvested just after fertilisation and incubated at 28.5 °C. Embryo lines used were: wild types (WT), Tg(beta-actin:mCherry-CAAX) (labelling membranes), Tg(beta-actin:Lifeact-eGFP) (labelling F-actin) and Tg(beta-actin:Myosin2-mCherry).

Bead and cell transplantation

Transplantations were at 1k-cell stage using a tip broken elongated capillary [] mounted on an oil filled pressurised system controlled by a syringe []. Beads or cells were transplanted at 1k-cell stage. Beads were incubated in 4% BSA before grafting to reduce chances of bead rejection when injected.

7.5 Discussion

The study presented here has demonstrated that, for the first time, a direct link between cell behaviours and embryo morphogenesis arising from changing mechanical properties. By applying a directed local force to a developing embryo through an embedded magnetic bead, local and ensemble mechanical properties of tissue were characterised. Working in the blastula, it was shown to have an intrinsic viscoelastic response; the data compounds that tissues exhibit fluid-like behaviours with similar studies using optical tweezers in mature epithelia, [19] and the use of magnetic droplets injected into much older fish than considered here [18]. The viscoelastic time scale remained as a constant across both time and embryonic mutations. The

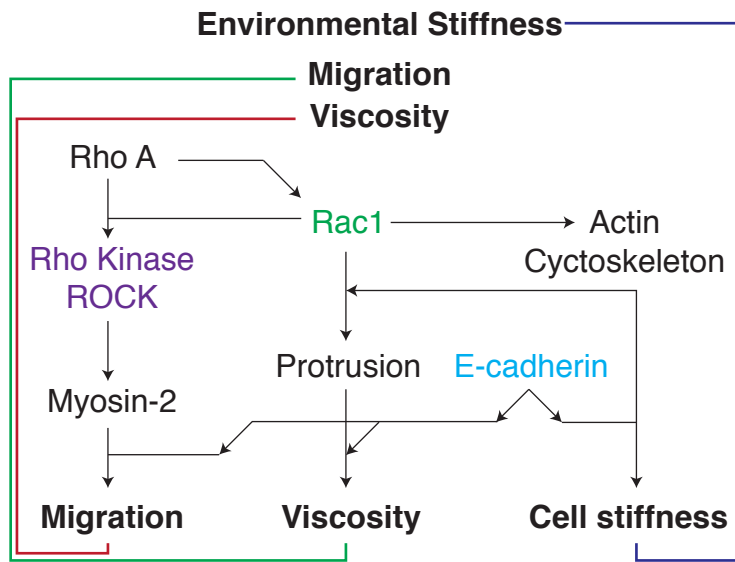


Fig. 7.9 Summary of effects of knockdowns in cell motion, cell protrusive activity and cell adhesion through the loss of function of Rac1, ROCK and E-Cadherin. Based on literature, a feedback mechanism via mechano-sensing through Rac1 (blue, red and green arrows) is speculated to regulate the tissue rheology. Rac1 activation promotes actin cytoskeleton elaboration, increasing cell stiffness, and the production of cell protrusions. Protrusions provide a means of elaborating cell-cell adhesion, increasing tissue viscosity and enabling motility. Motility is achieved by contraction relative to points of adhesion, providing both movement and effectively testing the mechanical compliance of the cell network, feeding back to activate Rac1.

results of this study provide elucidate the meaning of the rheological parameters. The viscous and elastic aspects are involved in cell shape and cell intercalation of the deformation. Larger stiffness is related with less deformable cells, and larger viscosity with diffusely of cells rearrangement. In developing wild-type embryos and prior to bulging the blastula becomes 3 fold more viscous and stiff.

Tissue viscosity in the form of cell rearrangement, is a measure of the friction imposed by cell-cell connections, which may be mediated by cell protrusions and E-cadherin adhesion. Rac1 activity would then follow to promote viscosity and cell stiffness by increasing polymerised action and encouraging cell-cell adhesions via E-cadherin connections. Yet, the decrease in cell stiffness with MoECad treatment suggests a more complicated coupling. We propose that a cellular mechanotransduction mechanism assays the environment's compliance between sites of adhesion. It is well understood that cells grown on a surface adjust their mechanical stiffness in proportion to substrate stiffness [(32, 33)]. In the case of early mesenchymal tissues, we suggest that the cells themselves collectively constitute their own local mechanical environment, coupled via protrusion promoted cell-cell adhesion. Numerous examples exist of mesenchymal cells interacting via protrusions. During collective migration, cadherin-mediated cell-cell connections are able to promote cell polarisation and cytoskeletal rearrangements, acting through Rac1 activation [(34)]. Given the role of protrusions in both motility and transduction, this relationship explains the close correlation between viscosity and stiffness.

The emergence of cohesive mesenchymal tissue mechanical properties may be linked with the motility of its cells, and in particular the formation of protrusions that facilitate the establishment of cadherin-based cell-cell adhesions. Connectivity could result in an actin superstructure networked between cells, through cell adhesion molecules. Tissue stiffness and viscosity are well correlated with the number of protrusions present. It is tempting to speculate that these mechanisms might be found in other mesenchymal tissues during development. These findings highlight a potentially fundamental difference in the determination of mechanical properties between epithelial and mesenchymal tissues. Epithelia representing relatively static configurations, based upon adhesion and contraction, while mesenchyme are adhesive and stiff but dependent upon dynamic protrusion-based motility. We speculate that the stiffening blastula, composed of radially-anisotropic cells, is thus poised to drive blastula thinning and yolk bulging in the next morphogenetic movement of the zebrafish embryo.

Analysis

All tests were performed with R software. A linear mixed effect model was performed to compare rheological parameter trends in different loss-of-function assays. Anova tests compared linear fits on developmental trends of the rheological parameters between WT and loss of function conditions. The percentage bend correlation method was used for correlation between cell and rheological parameters, to take in account outliers.

